ETH zürich

ETH Library

Self-camber of timber beams by swelling hardwood inlays for timber–concrete composite elements

Journal Article

Author(s):
Müller, Katharina; Grönquist, Philippe; Cao, Alex Sixie; Frangi, Andrea

Publication date:
2021-11-15

Permanent link:
https://doi.org/https://doi.org/10.3929/ethz-b-000508493

Rights / license:
Creative Commons Attribution-NonCommercial-NoDerivatives 4.0 International

Originally published in:
Construction and Building Materials 308, https://doi.org/10.1016/j.conbuildmat.2021.125024

This page was generated automatically upon download from the ETH Zurich Research Collection.
For more information, please consult the Terms of use.

Construction and Building Materials 308 (2021) 125024

Contents lists available at ScienceDirect

Construction and Building Materials

journal homepage: www.elsevier.com/locate/conbuildmat

Self-camber of timber beams by swelling hardwood inlays for timber–concrete composite elements

Katharina Müller[1], Philippe Grönquist[1,*], Alex Sixie Cao, Andrea Frangi

ETH Zurich, Institute of Structural Engineering, Timber Structures, Stefano-Franscini-Platz 5, 8093 Zürich, Switzerland

ARTICLE INFO

Keywords:
Self-camber
Timber
Wood swelling
Timber–concrete composite
Swelling pressure
Restrained swelling
Serviceability limit state
European beech

ABSTRACT

Timber–concrete composites (TCC) are smart solutions for slabs in residential and office buildings regarding the sustainable and performance-optimized use of materials. However, a non-negligible disadvantage is the deflection of the timber elements caused by in-situ concrete casting during construction. This paper presents an approach to camber timber elements without external forces by using the innate swelling capacity of wood. Oven-dried hardwood inlays can be inserted transversally into cuts on the top side of a timber element. After an increase of the moisture content in the inlays, the swelling pressure will result in a self-camber of the timber element. In this study, a procedure for prediction of the self-camber is derived and the model is validated using an experimental test series. The results demonstrate that the self-camber of spruce elements using beech inlays is both feasible and predictable. On this basis, practical application scenarios for TCC elements in timber engineering are shown and discussed.

1. Introduction

The increasing need for sustainable solutions in the construction industry brings the most common slab system with reinforced concrete in distress [1,2]. In Switzerland, reinforced concrete slabs account for the vast majority of all built slabs in residential and office buildings. However, the cement production is the third-largest human-made source of CO_2 emissions [3]. The typical density of reinforced concrete at $25\,kN/m^3$ is also a serious disadvantage regarding transport, installation, and loads on the foundations. For timber-only slab systems, the required stiffness for longer spans is often a challenge. The thickness of timber-only slabs significantly increases with the span to achieve the required load-bearing capacity, deflections benchmarks, and in some cases vibration and acoustic performance. Timber–concrete composite (TCC) slabs combine the advantages of both timber and concrete and bring them together to an optimized performance [4–6]. The timber part below acts as formwork and reinforcement for the concrete, taking up the tensile forces and optionally providing an aesthetic ceiling for the floor below. The concrete part on top takes up the compression forces, improving the fire resistance and enhancing the stiffness and mass of the slab for better vibration and acoustic behavior [7,8].

The main structural challenges of TCC slabs are the connection between timber and concrete [9] and the large deflections due to the complex long-term behavior over the entire service life [10–13]. The challenge of deflections does not only concern TCC slabs over the service life in a composite state, but also the initial state of the timber elements during in-situ concrete casting [14,15]. The deflection due to the load of the fresh concrete is a significant disadvantage during the construction state and constitutes a big portion of the total final deflections over the service life.

Apart from technical notes [16], no specific considerations are made in design standards with respect to camber measures. In practice, camber is often subtracted from the calculated total deflections. The hitherto available solutions to comply with the deflection guidelines are on-site propping, prefabrication, or external pre-bending or milling of the timber elements into a pre-camber shape. However, prefabrication is not always possible depending on the construction site and procedure or the transport and production possibilities. Therefore, propping is the most common as it is compatible with in-situ concrete casting and seemingly straightforward. However, many props are needed for larger spans and they severely interfere with the process on the construction site. Propping is also very time-consuming, as the props need to stay until the concrete has hardened and reached a sufficient strength to ensure the composite action. Furthermore, there are findings that propping does not solve the long-term deflection problem, since eigenstresses are built up during the propping phase [15]. These eigenstresses may increase the deflection behavior in the long-term perspective [17]. More practical methods exist, e.g. the cambering of timber elements

* Corresponding author.
E-mail address: groenquist@ibk.baug.ethz.ch (P. Grönquist).
[1] Contributed equally to this work.

https://doi.org/10.1016/j.conbuildmat.2021.125024
Received 31 March 2021; Received in revised form 25 August 2021; Accepted 21 September 2021
0950-0618/© 2021 The Authors. Published by Elsevier Ltd. This is an open access article under the CC BY-NC-ND license (http://creativecommons.org/licenses/by-nc-nd/4.0/).

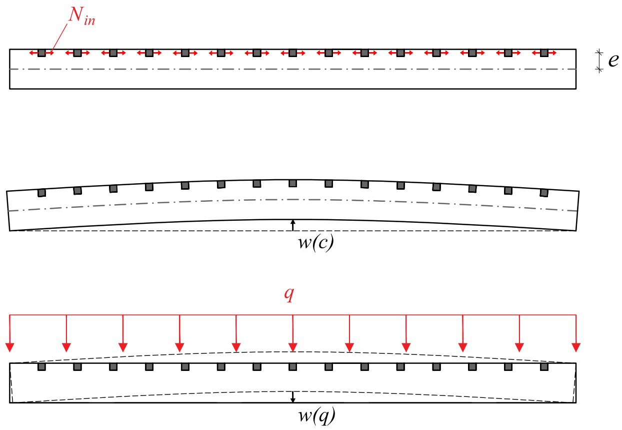

Fig. 1. Principle of self-camber of a simply supported timber beam by swelling inlays where each inlay generates a normal force N_{in}. A total self-camber of $w(c)$ can be used to compensate a deflection $w(q)$.

by using distributed screw fasteners inserted at an angle to the axes of the elements [18,19].

The innovative measure to compensate deflections of TCC elements presented in this paper does not require any external forces, can be carried out on site, and has a manageable expenditure of time and materials. The timber element is cambered by inserting oven-dry hardwood inlays into cuts or notches milled into the top surface of the timber element. The inlays expand while adjusting to the moisture content (MC) of the surrounding timber board and climate, inflicting an expansion force N_{in} eccentric to the longitudinal axis of the element (Fig. 1). The eccentricity e leads to a moment M in the timber element at the inlay region:

$$M = N_{in} \cdot e. \tag{1}$$

This moment leads to a curvature $\chi = M(EI_r)^{-1}$, which for a simply supported beam, assuming that the moment is sustained over the whole span of the beam, will lead to an upwards deflection $w(c)$ at mid-span of

$$w(c) = \frac{\chi l^2}{8} = \frac{N_{in} \cdot e \cdot l^2}{8EI_r}. \tag{2}$$

Hereby l is the span, and EI_r is the flexural rigidity of the notched timber beam, with a reduced area moment of inertia I_r due to the notches. The self-camber deflection $w(c)$ can now be used to compensate deflections $w(q)$ due to a loading q of the beam as illustrated in Fig. 1.

In order to efficiently employ this principle, i.e. to maximize $w(c)$, it is apparent that next to the number of inlays and their eccentricity, the generated swelling forces N_{in} need to be maximized. Previous works [20–22] have used the set-recovery capacity [23] of densified wood inlays to generate a large pre-stress in timber beams. However, in the study of Grönquist et al. [24], where swelling pressure of densified and native European beech wood was compared, it was shown that native beech wood could also reach sufficiently high swelling pressures compared to densified wood. This renders an additional and expensive densification process of the inlays unnecessary. A related numerical parametric study on the concept of self-camber for TCC elements demonstrated that in dependence of geometric configuration, any practically relevant target camber $w(q)$ can be achieved by using native European beech wood [25].

A further challenge of the self-camber principle is to achieve a precise prediction by calculation models. Otherwise, a given inlay configuration is uncertain with respect to optimally compensating for $w(q)$. Eq. (2) shows that $w(c)$ is directly proportional to N_{in}, highlighting its importance in terms of accuracy of prediction. However, as the generated swelling pressure between inlay and beam (and therefore its resultant N_{in}) is highly uncertain in terms of a material perspective, this parameter needs to be precisely analyzed and assessed. Specifically, it is known that wood possesses a complex load-, time-, and moisture-dependent mechanical behavior that can be summarized and modeled as a rheological one [26,27]. Mechanisms such as hardening after yield, or relaxation should be considered. Therefore, a precise but practical model for determination of the swelling pressure is necessary.

In this study, an analytical and simple model for the estimation of $w(c)$ is derived. The model considers moisture-dependent elastic, yielding, and hardening properties of the inlay material. The swelling against the elastic embedding case, annual ring inclination in the inlays, as well as reduction of flexural rigidity due to notches of the timber beam are considered. The model is validated against experimental data from three self-cambering specimens of 2 m span and with different notch configurations. A detailed discussion is provided on how to reach the maximum swelling pressure, and a sensitivity analysis is conducted in order to quantify the required control over manufacturing parameters. Finally, practical approaches for use of the self-camber concept in timber engineering are discussed by showing how the deflections in different states of 4, 6, and 8 m spanning TCC slabs can be compensated by self-camber.

2. Calculation of self-camber

In the following subsections, a step-by-step approach to calculate the value of the self-camber $w(c)$ in dependence of the beam and inlay geometry and their material parameters is derived and presented. The model approach is shown in Fig. 2.

2.1. Effective swelling coefficient and modulus of elasticity of inlay

While the grain direction of the inlay should always be perpendicular to the beam's grain direction because of otherwise insufficient swelling, it is often impossible to realize a clean tangential or radial orientation of the inlays. Practically, growth ring curvature or unclean cutting and preparation of the inlays results in an inclination θ of the wood's anatomical T direction with respect to the beam axial direction. For this reason, and in order to provide properties in the beam's axial direction, the effective inlay differential swelling coefficient α_{in} and the effective modulus of elasticity of the inlay E_{in} can be approximated by

$$\alpha_{in} = \alpha_T \cos^2\theta + \alpha_R \sin^2\theta, \tag{3}$$

$$E_{in} = \frac{E_T E_R}{E_T \sin^2\theta + E_R \cos^2\theta}, \tag{4}$$

where the indices T and R indicate the properties in strict tangential and radial directions of the inlays. In Eq. (3), the effective swelling coefficient α_i is calculated by tensor rotation. In Eq. (4), the effective modulus of elasticity E_i can be calculated using Hankinson's formula [28] in order to avoid the need of specifying the shear modulus and Poisson's ratio of the inlays.

2.2. Linear elastic swelling pressure

By considering the restrained swelling of an inlay with length l_{in} in an elastic embedding represented by a unit zone of the surrounding beam of length l_u, where $l_u = d + l_{in}$ with d being the distance between inlays, the following governing equilibrium differential equation can be formulated for the 1D case:

$$\frac{d}{dx}\left(\left(\frac{du}{dx} + \varepsilon_0\right) E_{in} A_{in}\right) = 0. \tag{5}$$

Hereby, x is the position variable, u is the displacement of the inlay along x, A_{in} is the cross-sectional area of the inlay, and $\varepsilon_0 = \alpha_{in}\Delta\omega$ is the

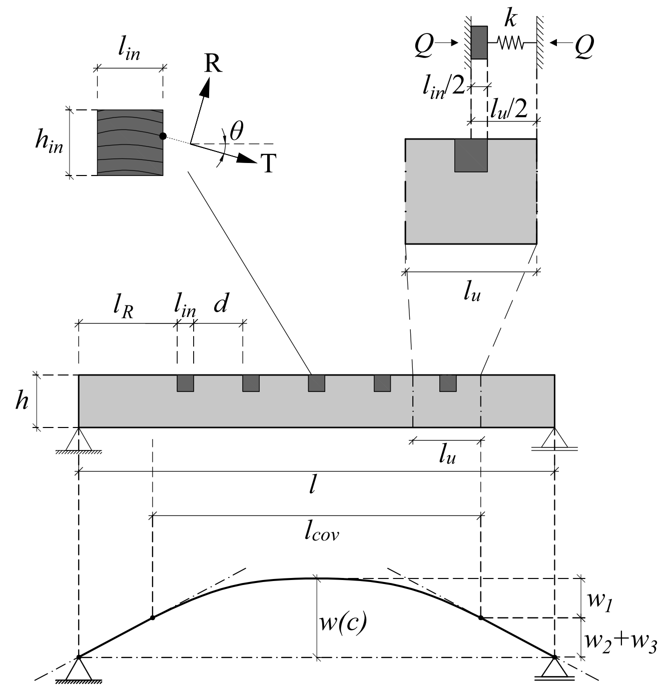

Fig. 2. Schematic model of a beam with inlays and the induced self-camber $w(c)$.

residual strain due to swelling of the inlay with expansion coefficient α_{in} and an applied moisture content difference of $\Delta\omega$. By integrating Eq. (5) once and twice, the following expressions can be obtained:

$$E_{in}A_{in}\frac{du}{dx} + E_{in}A_{in}\varepsilon_0 = C_1, \tag{6}$$

$$E_{in}A_{in}u + E_{in}A_{in}\varepsilon_0 x = C_1 x + C_2, \tag{7}$$

where C_1 and C_2 are integration constants. Eq. (6) is the first integration of Eq. (5) and equals the resulting load Q acting on the cross-section of the inlay. By formulating the boundary conditions in Eqs. (6) and (7) as $u(x=0)=0$ and $Q(x=(l_{in}/2)) = -ku(x=(l_{in}/2))$, where $k = E_b A_{in}((l_u/2)-(l_{in}/2))^{-1}$ is the equivalent spring stiffness representing the elastic embedding around the inlay (with modulus of elasticity of the beam E_b), we obtain

$$C_2 = 0, \tag{8}$$

$$C_1 = Q = \frac{k(l_{in}/2)\varepsilon_0}{1 + k(l_{in}/2)(E_{in}A_{in})^{-1}}. \tag{9}$$

By inserting the expressions for the equivalent spring stiffness k and the residual strain ε_0, and by dividing the resulting load Q by the inlay area A_{in}, we obtain the swelling pressure σ_x as:

$$\sigma_x = \left(\frac{l_u - l_{in}}{E_b l_{in}} + \frac{1}{E_{in}}\right)^{-1}\alpha_{in}\Delta\omega. \tag{10}$$

Finally, the swelling pressure resultant per unit width for an inlay can be calculated with $N_{in} = \sigma_x h_{in}$, where h_{in} is the inlay height and where it is assumed that the 1D swelling pressure is constant over the inlay height. It should be noted that in the case of an infinitely soft embedding of the inlay (i.e. $E_b \to 0$) $N_{in} = 0$, and in the case of an infinitely stiff embedding (i.e. $E_b \to \infty$) $N_{in} = E_{in}\alpha_{in}\Delta\omega h_{in}$.

2.3. Swelling pressure limited by yield and hardening of inlay

The case of linear elastic swelling pressure, like above, is an ideal simplification omitting the fact that the maximum possible swelling pressure is physically limited. Transversally compressed wood at the macroscopic scale shows a gradual and distinct softening behavior with increasing level of compression [29]. Mathematically, the Ramberg–Osgood (RO) function [30] provides a convenient representation of the stress–strain relationship of transversally loaded hardwood; especially, in the case of European beech [29]. The RO function,

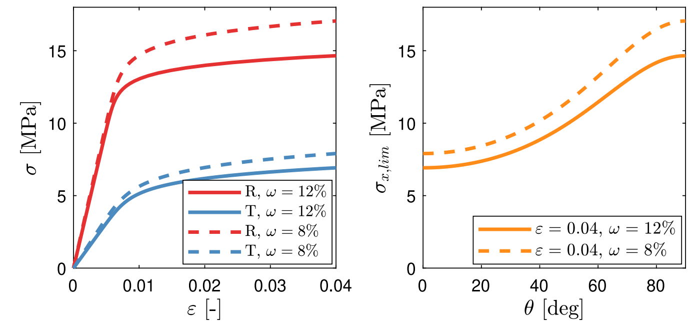

Fig. 3. Left: RO curves for compression of European beech wood in T and R directions for two exemplary levels of MC ($\omega = 8\%$ and $\omega = 12\%$), based on data from [29]. Right: Hankinson formula (Eq. (4)) applied to theoretical values of $\sigma_{x,lim}$ after $\varepsilon = 0.04$ (for a T orientation of an inlay, i.e. $\theta = 0$, this corresponds to a swelling strain resulting from a moisture change of approx. $\Delta\omega = 10\%$).

$$\varepsilon = \frac{\sigma}{E_i} + \left(\frac{\sigma}{K_i}\right)^{n_i}, \tag{11}$$

possesses 3 parameters, E_i, K_i, and n_i where the index i is the radial direction R or the tangential direction T of the wood. Examples for the values of these parameters for European beech are given in Table 2 and exemplary curves are shown in Fig. 3. Practically, in order to be useful in the context of maximum admissible swelling pressure, the RO function needs to be inverted. However, since it is not invertible, an approximate first-order solution for the inverse RO function, following [31], can be used as follows:

$$\sigma_{i,lim} \approx \frac{K_i(\alpha_i\Delta\omega)^{n_i}}{1 + K_i E_i^{-1} n_i (\alpha_i\Delta\omega)^{n_i - 1}}. \tag{12}$$

With the above equation, the swelling strain $\alpha_i\Delta\omega$ can be directly used to calculate the maximum possible swelling pressure $\sigma_{i,lim}$ in the anatomical directions $i = R$ and $i = T$. By calculating both $\sigma_{R,lim}$ and $\sigma_{T,lim}$, one can presumably apply the Hankinson formula (Eq. (4)) again in case of inclined annual rings of an inlay and find the maximum admissible swelling pressure $\sigma_{x,lim}$ (see Fig. 3). The true value of the swelling pressure resultant can now be calculated using the condition

$$N_{in} = \min(\sigma_x, \sigma_{x,lim})h_{in}. \tag{13}$$

The condition assures that the generated normal force by the restrained swelling of the inlay against the elastic embedding is adequately limited by possible yield of the inlay.

2.4. Reduced area moment of inertia of notched beam

In a next step, the influence of the notches on the flexural rigidity of the timber beam has to be quantified. For this, a reduced area moment of inertia is calculated for the notched part of the beam shown as l_{cov} in Fig. 2. By assuming small deflections and that the notched part h_{in} of the cross-section is in a uniform stress state caused by the swelling pressure of the inlays, the weighted average axial stiffness of the notched part of the cross-section $E_b A_{r,in}$ can be expressed as

$$E_b A_{r,in} = \frac{E_b A_{in} l_{in} + E_{in} A_{in} d}{l_{in} + d}, \tag{14}$$

where $A_{r,in}$ is the reduced or effective cross-section area of the notched part. By re-arranging Eq. (14), the following expression is obtained:

$$A_{r,in} = \frac{E_b l_{in} + E_{in} d}{E_b(l_{in}+d)} A_{in} = \beta A_{in}, \tag{15a}$$

$$\beta = \frac{E_b l_{in} + E_{in} d}{E_b (l_{in} + d)}. \tag{15b}$$

In Eq. (15a), β is a reduction factor. Since the width of the notches and the beam is identical, Eq. (15a) reduces to $h_{r,in} = \beta \cdot h_{in}$. The reduced area moment of inertia for the rectangular beam with inlays can now be expressed as

$$I_r = \frac{1}{12} b(h - (1-\beta)h_{in})^3, \tag{16}$$

where b is the width of the beam. Finally, the curvature of the notched part of the beam can be expressed as:

$$\chi = \frac{N_{in}}{E_b I_r} \frac{h}{2}. \tag{17}$$

In Eq. (17), it is assumed that the eccentricity has a constant value of $e = h_{in}/2 + (h - h_{in})/2 \approx h/2$. Theoretically, the centroid of the beam will be slightly different due to the reduced stiffness of the notched part. In most cases, the movement of the centroid is very small and is therefore neglected. However, this cannot be generalized, and in some situations, will need to be considered.

2.5. Self-camber of a simply supported beam

The self camber at mid-span of a beam fully covered with inlay units can be expressed as:

$$w_{cov} = \frac{\chi l_{cov}^2}{8}, \tag{18}$$

where $l_{cov} = n l_u$ is a multiple of l_u and represents the length of the beam covered by n inlay units. Due to practical reasons, it may be desirable to keep the regions around the supports of the beam free of notches (see 4.4). Therefore, the first inlays may be separated from the beam edges by a distance l_R for a beam with span l. The resulting self-camber of the beam can be decomposed into three parts:

$$w(c) = w_1 + w_2 + w_3 \tag{19}$$

where w_1 is the deflection of the notched length of the beam l_{cov}, w_2 is the deflection due to rigid body motion of the support regions without notches, and w_3 is the deflection of the support regions due to bending. w_3 is idealized as a cantilever beam with a moment at its free tip. w_1, w_2, and w_3 can be expressed as:

$$w_1 = w_{cov} = \frac{\chi l_{cov}^2}{8}, \tag{20a}$$

$$w_2 = \frac{\chi l_{cov}}{2} \cdot (l_R - l_u) \cdot 2, \tag{20b}$$

$$w_3 = \frac{\chi (l_R - l_u)^2}{2}. \tag{20c}$$

3. Materials and methods

3.1. Experimental self-camber of 2 m span beams

Three single boards of 2 m span with different arrangements of the cuts as shown in Figs. 4 and 5 were tested. The specimens S1–S3 consisted of spruce boards (*Picea abies*) with cuts on the top side, where oven-dried European beech (*Fagus sylvatica*) inlays were placed. An optimal shape of the cuts and their arrangement in the timber boards was previously determined in a parametric study using a finite element model [25]. For each of the three specimens, a total of 15 cuts was chosen. The specimens differ only in distances between the cuts d and distances to the edge l_R. Table 1 shows the detailed characteristics of the three specimens. The spruce boards were manufactured with a length of 2000 mm, a width of 40 mm, and a height of 80 mm. The cuts on

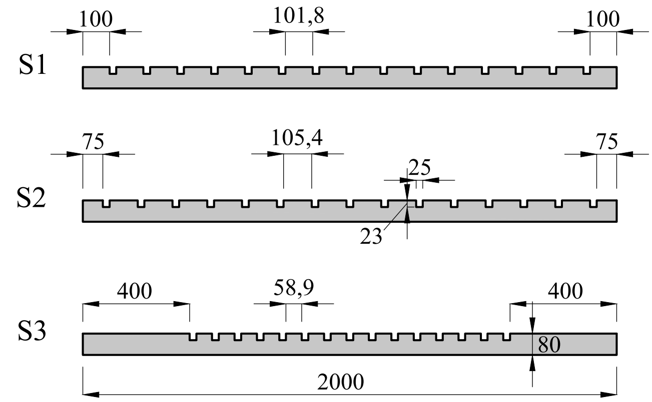

Fig. 4. Dimensions and configuration of specimens S1–S3.

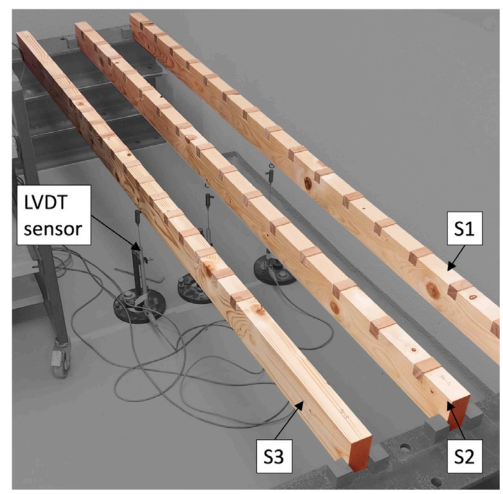

Fig. 5. Image of specimens S1–S3 with measurement of upwards deflection by suspended LVDT sensors in 65% RH and 20 °C climate chamber.

the top side of the boards were milled out using a circular saw blade. The boards were then acclimatized in a 65% relative humidity (RH) and 20 °C climate. After a month in the climate, the width of each cut was then manually measured using a digital caliper (precision of ±0.01 mm). Meanwhile, the beech inlays were oven-dried for 4 days at 103 °C. After drying, the width of each inlay was adjusted using a thickness planer (tolerance of ±0.1 mm) to match the exact width of each single cut the inlays were to be placed in. Overall, the cuts had an average width of 25 mm and an average depth of 23 mm. The inlays were inserted so that the anatomical T direction aligned with the span direction of the board. For each specimen (S1, S2, and S3) the inlays had an average annual ring inclination of 10° off from the T direction. After inserting the inlays into the cuts, the boards were left in the 65% RH and 20 °C climate for the inlays to swell. Over a period of 120 h, the vertical upwards deflection of the three boards was measured using linear variable differential transformer (LVDT) sensors (resolution of 10^{-5} mm). During the measurement, the boards were simply supported at each end.

3.2. Model calculation of experimental configurations

The analytical model presented in Section 2 was used to calculate the self-camber $w(c)$ achieved by the experimental samples S1–S3. Therefore, the geometry input parameters used for the modeling corresponded to the values given in Table 1. The material parameters for the beech inlays corresponded to the RO parameters as shown in Table 2.

Table 1
Geometrical configurations of the three specimens S1, S2, and S3.

Parameter	Label	Unit	Specimens		
			S1	S2	S3
Span	l	[mm]	2000	2000	2000
Height	h	[mm]	80	80	80
Width	b	[mm]	40	40	40
No. of cuts and inlays	n	[mm]	15	15	15
Distances between cuts	d	[mm]	101.8	105.4	58.9
Distances to edge	l_R	[mm]	100	75	400
Length of cuts and inlays	l_{in}	[mm]	25	25	25
Depth of cuts and inlays	h_{in}	[mm]	23	23	23

Table 2
Parameters for calculation of moisture-dependent RO curves for tangential and radial direction of beech inlays under compression stress. Properties calculate as $P(\omega) = m\omega + q$ where ω is the moisture content in %. Properties are valid in a range of $\omega = 6\%$ to $\omega = 14\%$. Parameters based on data from [29].

Parameter	E_R [MPa]	K_R [MPa]	n_R [–]	E_T [MPa]	K_T [MPa]	n_T [–]
m	−21.4	−0.908	0.5871	−17.62	−0.548	0.3333
q	2176.4	28.271	9.6429	833.29	16.664	5.4000

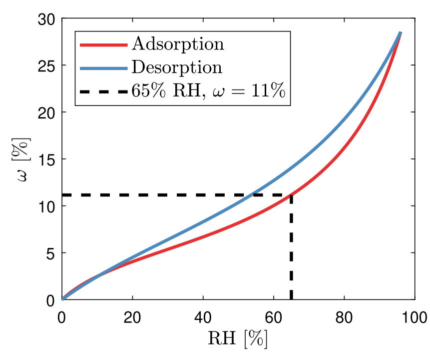

Fig. 6. Adsorption and desorption isotherms for European beech wood at 20 °C: Wood equilibrium moisture content (ω) vs. relative air humidity (RH). Black dashed lines represent adsorption conditions at 65% RH and 20 °C climate. Sorption curves based on Hailwood–Horrobin model data according to [32].

The swelling coefficients in R and T directions of the inlays, needed for Eq. (3), were chosen as $\alpha_R = 0.0018\%^{-1}$ and $\alpha_T = 0.0040\%^{-1}$, and the average value of the annual ring inclination off from the insertion axis (T axis) was $\theta = 10°$. According to the adsorption isotherm curve for European beech shown in Fig. 6 (adopted from [32]), the applied difference in MC of the inlays was $\Delta\omega = 11\%$. Finally, the modulus of elasticity of the spruce boards was assumed to be $E_b = 11'000$ MPa, according to the value given for the timber grading class C24 following [33].

3.3. Sensitivity analysis

The analytical model of Section 2 was used for a sensitivity analysis. Assuming that each model input parameter X_i is following a certain probability density function (PDF) with specific parameters, the model output random vector ($\mathbf{Y}$) can be quantitatively assessed by Monte-Carlo sampling where $\mathbf{Y} = \mathcal{M}(\mathbf{X})$, such that $\mathcal{M}$ is the computational model and $\mathbf{X}$ is an input vector containing an independent random sampling of each input parameter X_i. The procedure allows to calculate the partial variances of each of the model input parameters separately and of their combination with respect to the variance of $\mathbf{Y}$. In this study, the Sobol' indices method [34], a global-type sensitivity analysis method was employed in order to quantify the contribution of variability of each input parameter to the resulting variability of the self-camber.

The sensitivity analysis was conducted on the exemplary situation of the specimen S3. The model input parameters were separated in fixed parameters and in parameters with attributed uncertainty. The latter category was subdivided into two subcategories of manufacturing parameters and material parameters. The manufacturing parameters were chosen as the MC difference $\Delta\omega$, the inlay annual ring inclination θ, and a newly introduced parameter, the machining tolerance c. The tolerance c was defined in the frame of the model of Section 2 such that c is representing a clearance between inlay and notch. Over the length of c, the inlay is subject to free swelling with no contribution to the swelling pressure. Therefore, an equivalent MC difference $\Delta\omega_{eq} = c(l_{in} - c)^{-1}\alpha_{in}^{-1}$ was defined that is to be subtracted to $\Delta\omega$ in order to calculate the self-camber. The other subcategory of material parameters contains the inlay swelling coefficients (α_T, α_R) and the moduli of elasticity of the inlay and the spruce beam ($E_{T,q} = E_T(\omega = 0)$, $E_{R,q} = E_R(\omega = 0)$, E_b). The model input parameters and their chosen distributions are shown in Table 3. Four different scenarios of parameter combination were analyzed:

Table 3
Model input parameters X_i attributed with uncertainty for sensitivity analysis of specimen S3 situation (fixed parameters according to Table 1). Manufacturing parameters (c, $\Delta\omega$, θ) were attributed with uniform ($\mathcal{U}$) probability density functions (PDF) with lower an upper bounds a and b, and material parameters (α_T, α_R, $E_{T,q} = E_T(\omega = 0)$, $E_{R,q} = E_R(\omega = 0)$, E_b) with lognormal ($\mathcal{LN}$) PDFs with mean values μ and coefficients of variation (COV).

X_i	Unit	PDF	Scenario parameters			
			A	B	C	D
c	[mm]	$\mathcal{U}[a,b]$	[0, 0.5]	[0, 1]	[0, 0.5]	[0, 1]
$\Delta\omega$	[%]	$\mathcal{U}[a,b]$	[10, 12]	[9, 13]	[9, 13]	[10, 12]
θ	[deg]	$\mathcal{U}[a,b]$	[0, 15]	[0, 45]	[0, 25]	[0, 25]
α_T	[%$^{-1}$]	$\mathcal{LN}[\mu, COV]$	[0.0040, 10%]			
α_R	[%$^{-1}$]	$\mathcal{LN}[\mu, COV]$	[0.0018, 10%]			
$E_{T,q}$	[MPa]	$\mathcal{LN}[\mu, COV]$	[833.29, 10%]			
$E_{R,q}$	[MPa]	$\mathcal{LN}[\mu, COV]$	[2'176.4, 10%]			
E_b	[MPa]	$\mathcal{LN}[\mu, COV]$	[11'000, 10%]			

- Scenario A: High control possibility over all of the manufacturing parameters.
- Scenario B: Low control possibility over all of the manufacturing parameters.
- Scenario C: High control over machining tolerance, low control over climate, moderate control over inlay orientation.
- Scenario D: Low control over machining tolerance, high control over climate, moderate control over inlay orientation.

For each scenario, the model was evaluated 10^7 times and only first order Sobol' indices were considered. For simplicity, it was assumed that all input variables are independent and that the material parameters each possess a fixed coefficient of variation (COV) of 10% independently of the scenario. The sensitivity analysis was conducted with *UQlab* [35,36], an uncertainty quantification tool for Matlab.

4. Results and discussion

4.1. Experimental validation of model

The amount of self-camber $w(c)$, i.e. upwards deflection reached over time by the specimens S1–S3 is shown in Fig. 7. It can be recognized that all three specimens reached a limit value at a time of 48 h of being in a 65% RH climate. After a gradual increase in $w(c)$, specimens S1 and S2 reached a value of about 10 mm each, whereas specimen S3 reached a value of approximately 13.7 mm. The limit values of the specimens along with the model predictions using the presented model of Section 2 are shown in Table 4 (and Fig. 7). The accuracy of the analytical model for all three specimens is fairly reasonable and inside a range of precision that can be justified by the natural variability in material parameters. The specimen data shows that the deflection for specimen S2 is slightly larger than for S1. However, the model shows

Table 4
Self-camber deflections calculated by analytical model (Eq. (19), rounded values) compared to data from experiments (rounded max. values from Fig. 7).

Deflection	S1		S2		S3	
	Model [mm]	Data [mm]	Model [mm]	Data [mm]	Model [mm]	Data [mm]
$w(c)$	8.97	9.70	8.50	9.96	13.37	13.65
w_1	7.77		8.17		3.71	
w_2	1.20		0.33		8.45	
w_3	0.01		0.001		1.20	

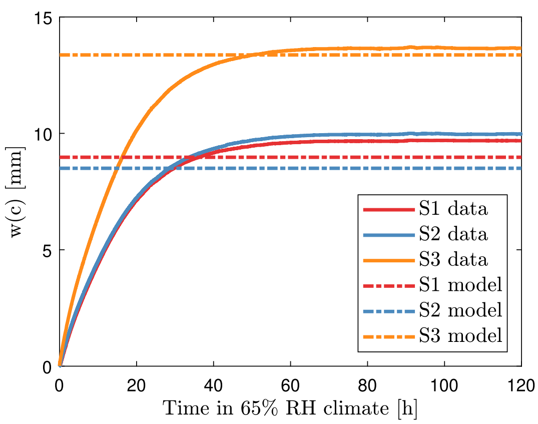

Fig. 7. Self-camber of specimens S1–S3 in 65% RH climate ($\Delta\omega \approx 11\%$). Comparison of analytical model (dashed lines) and measured data of the specimens (full lines).

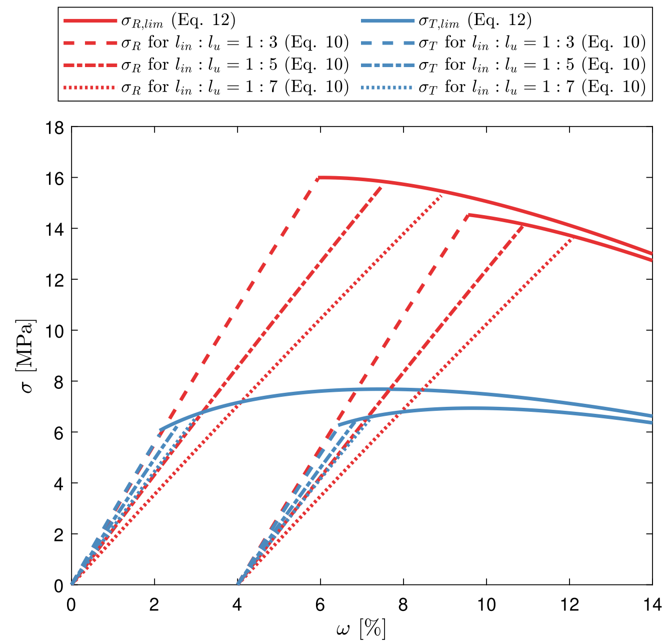

Fig. 8. Swelling pressure as calculated by analytical model using moisture-dependent elastic embedding curves (Eq. (10), assuming $E_b = 11'000$ MPa) and inverse RO curves (Eq. (12)) for R and T orientations of inlay made from European beech. Different lines with different starting MC's ($\omega = 0$ and $\omega = 4\%$) show pressure evolution over respective moisture uptake until $\omega = 14\%$. Elastic embedding curves are shown for three exemplary situations of inlay spacing: $l_{in} : l_u = 1:3$, $1:5$, and $1:7$. *Example: Inserting an R-oriented inlay ($\theta = 90°$) at an initial MC of 0% (oven-dry state) will result in a maximal pressure of about 16* MPa *at around $\omega = 6\%$. A further moisture uptake of the inlay until $\omega = 14\%$ will result in a reduction of the pressure to about 13* MPa.

the opposite behavior. The difference is very slight, and therefore, may be attributed to material variability in the specimens too. It can be concluded that the prediction model shown in Section 2 is suitable for predicting the final value of self-camber of notched spruce beams with beech inlays.

In Table 4, the decomposition of the total model self-camber $w(c)$ into w_1, w_2, and w_3 is shown. The deflections from the notched length of the beam (w_1) is the largest in S2. This is as expected as S2 has the largest share of notched length compared to the other specimens. For S3, the largest portion of the deflections results from the rigid-body motion of the support regions of the specimen (w_2). This is reasonable as the support regions in this specimen are much larger than in the other specimens. The flexural deflections from the support regions (w_3) of the beams are reasonable in all three specimens, where longer support regions without notches are in theory subject to larger flexural deflections.

Self-cambering, as will be shown in Section 5, is necessary for larger spans (> 4 m). However, in order to validate the presented model and for the objectives of this proof-of-concept study, the medium-scale approach with 2 m span beams was economic and straightforward (e.g. could be conducted in a controlled climatic chamber) while still being comparable to the spans in practice. The size effect between different spans is expected to be small. The axial force, and thus the moment induced by the swelling inlays in the beam, is in principal only dependent on the swelling pressure that can be reached by the inlays. The resulting self-camber $w(c)$ is dependent more on support conditions, positioning of the notches along the beam length, and geometry of the beam.

4.2. Analysis of swelling pressure

Next to predicting the value of $w(c)$ for any possible geometrical configuration according to Section 2, the validated model can now be used to conduct parametric analyses in order to identify optimal configurations and boundary conditions. As a principal goal, one may define reaching a maximal value of $w(c)$. Such an analysis is best conducted in an independent manner of specific inlay geometry parameters such as inlay height or length. As mentioned above and from Section 2, it is evident that $w(c)$ is directly proportional to the swelling pressure, which was defined as $\sigma = \min(\sigma_x, \sigma_{x,lim})$ in Eq. (13), where the subscript x is the orientation variable. To influence σ, one can vary the inlay orientation (θ) and the MC difference $\Delta\omega$. The inlay orientation will define the inlay swelling coefficient, the inlay modulus of elasticity, and the inlay RO parameters. Note that the MC difference is not to be treated as an absolute value but is the difference of a defined starting and end MC. Both the starting and end MC define the moisture range that characterizes the moisture dependent modulus of elasticity and RO properties of the inlay, which are variable over the time the inlay takes up moisture and swells. Finally, the last parameter influencing σ is the inlay spacing. The latter can be defined as a ratio of inlay length to inlay unit length ($l_{in} : l_u$), and influences the value of σ during the phase of swelling against elastic embedding. A parametric analysis of σ is shown in Fig. 8 for two orientations (R, $\theta = 90°$, and T, $\theta = 0$), two starting MCs ($\omega = 0$ and $\omega = 4\%$) with a final MC of 14%, and for three different inlay spacings $l_{in} : l_u = 1:3$, $1:5$, and $1:7$.

It can be observed that for both R and T orientations of the inlays, the elastic phase is similar. This is best explained by the fact that a T-oriented inlay possesses a higher swelling coefficient, but possesses a lower modulus of elasticity than an R-oriented inlay. This results in a perfect compensation making both initial slopes similar to one-another. However, for a T-orientation, the yield limit sets in much earlier than for an R-orientation. This enables R-oriented inlays to reach up to 16 MPa of swelling pressure while T-oriented inlays are limited to reach approximately half as much. An interesting behavior that can be observed is that T-oriented inlays seem to be able to activate the hardening phase of the RO curve while R-oriented inlays, upon reaching yield, continuously soften because of the stiffness loss due to moisture-dependency of the RO parameters. This leads to the insight that R-oriented inlay possess a distinct maximum value of σ directly when reaching the yield value. Therefore, a further moisture uptake is unnecessary, and an optimal difference in MC can be decided upon. For example, Fig. 8 shows that inserting R-oriented inlays at the oven-dry state and making them equilibrate at $\omega = 14\%$ (i.e. $\Delta\omega = 14\%$) will result in a lower value of σ than inserting inlays at 4% and then equilibrating them at 9% (i.e. $\Delta\omega = 5\%$ only). However, in order to reach high MCs, there is a tendency that the dryer the inlays are inserted, the higher the end value of σ. In addition, oven-drying the inlays is one of the only ways to practically reach low but defined MCs (in this case $\omega = 0$), while it is more difficult to reach other starting values because of the necessary equilibration in a defined dry climate. Finally, it can be recognized that whether the inlay spacing is narrow ($l_{in} : l_u = 1 : 3$, approximately as in sample S3) or wide ($l_{in} : l_u = 1 : 5$, approximately as in sample S2) only influences σ for low values of $\Delta\omega$ before the yield phase. However, in the example of R-oriented inlays inserted at oven-dry state and subjected to $\Delta\omega \approx 6\%$, the spacing $l_{in} : l_u = 1 : 3$ is able to reach $\sigma \approx 16$ MPa, but the spacing $l_{in} : l_u = 1 : 7$ only reaches $\sigma \approx 10$ MPa. However, upon reaching the moisture-dependent yield value, they fall on the same RO curve when $\Delta\omega$ is increased. As an overall conclusion, it can be said that an R-orientation of the inlay subjected to a limited change in MC will be able to maximize the swelling pressure, and thus also the self-camber $w(c)$.

Comparing to Section 4.1, it can be recognized that in Fig. 7 the experimental values of S1–S3 continuously increase, then stay constant after t = 48 h while the model in Fig. 8 shows that swelling pressure decreases after $\omega \approx 7\%$ in the situation of T-oriented inlays with $\theta \approx 10°$. The explanation may be the complex moisture diffusion process that results in the outer parts of the inlay being already in the decreasing phase while the inner, still dry parts are in the increasing phase of the σ curve. This moisture gradient likely results in an overall loss of stiffness of the rising phase in the experimental $w(c)$ versus time curve instead of in a distinct increase and decrease of $w(c)$. At $t = 48$ h, all the inlay cross-section has reached its final MC of $\omega \approx 11\%$.

4.3. Model limitations

The model presented in Section 2 has certain limitations that need to be taken into account. In a general sense, it is one-dimensional and uses approximation functions such as the Hankinson formula. A detailed 3D stress analysis would be possible by using a finite element numerical model. However, it is not the aim of this practically-oriented study to do so. From the material parameter perspective one needs to take into account that the used RO curves for transversal behavior of beech wood are experimentally valid only in a range of $\omega = 6\%$ to $\omega = 14\%$ [29]. This might lead to potential errors in the curves of Fig. 8 below $\omega = 6\%$. Furthermore, RO curves solely capture and model the linear-elastic, plastic, and hardening phases of the inlay material and neglect time-dependent deformation mechanisms. Time- and moisture dependent creep are neglected in the model due to complexity. These additional effects will lead to dissipation of a part of the available mechanical energy created by the constrained swelling, resulting in a potential reduction of swelling pressure and eventually self-camber. Therefore, even though the model could be validated for the experimental samples S1–S3, the authors advise to assess its usefulness with respect to the many simplifications and assumptions made and presented in Section 2.

4.4. Sensitivity analysis and practical limitations

The results of the sensitivity analysis are shown in Fig. 9 for each of the four manufacturing control scenarios A–D. For scenario A — high control over manufacturing parameters (total machining tolerance ≤ 0.5 mm, MC-control of ± 1%, inlay inclination 0–15°) — the Monte-Carlo sampling resulted in rather narrow distribution of self-camber with a mean value of $\mu = 12.89$ mm and $COV = 10.5\%$. The parameter

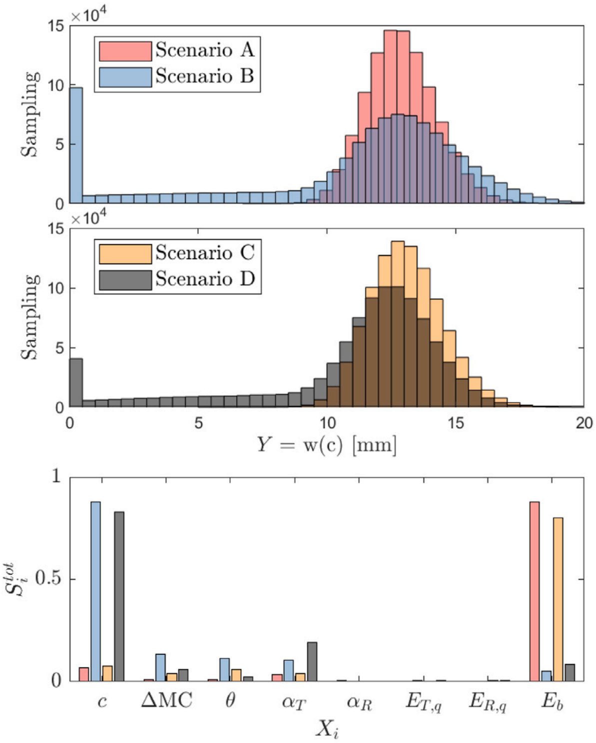

Fig. 9. Results of sensitivity analyses of four manufacturing control scenarios (A-D) for specimen situation S3. Top: Monte-Carlo sampling of self-camber random response vector **Y**. Bottom: Total Sobol' indices (S_i^{tot}) for each input random variable X_i for each scenario, see Table 3.

with the highest sensitivity, i.e. highest value of total Sobol' index S_i^{tot}, is the modulus of elasticity of the spruce beam E_b, while all of the other parameters seem unimportant. In contrast, scenario B — low control over manufacturing parameters (total machining tolerance ≤ 1 mm, MC-control of ± 2%, inlay inclination 0–45°) — the Monte-Carlo sampling resulted in rather broad distribution of self-camber with a mean value of $\mu = 10.79$ mm and $COV = 46.2\%$. It can be recognized that in some cases, no self-camber can be reached ($w(c) = 0$). This is most likely due to a particular combination of random input parameters such that the inlay is not able to exert any swelling pressure, e.g. in cases where the machining tolerance leaves the inlay with clearance gaps close to $c = 1$ mm, and simultaneously, low values of swelling coefficients and lower values of MC-difference. Effectively, in scenario B, the most sensitive parameter is c, while a minor importance can be attributed to $\Delta\omega$, θ, and α_T, and while the other parameters can be neglected.

For scenario C — High control over machining tolerance, low control over climate, moderate control over inlay orientation — a similar situation results as for scenario A. The Monte-Carlo sampling resulted in rather narrow distribution of self-camber with a mean value of $\mu = 13.09$ mm and $COV = 11.0\%$. Here again, the parameter with the highest sensitivity is E_b, while the other parameters seem unimportant. Finally, for scenario D — low control over machining tolerance, high control over climate, moderate control over inlay orientation — a similar situation results as for scenario B, with a mean value of $\mu = 10.97$ mm and $COV = 34.9\%$. Again, the most sensitive parameter is the clearance value c. This shows that even for a relatively good control over the climate conditions during production, the machining tolerance is still the decisive parameter.

In summary, it can be recognized that for the concept of self-camber to work in practice, an acceptable machining tolerance is approximately ≤ 0.5 mm. But even in that case, a good sorting (homogeneity) of board quality and a good knowledge of the modulus of elasticity, here for the spruce board, is necessary in order to be able to accurately predict the value of self-camber using the model presented in Section 2.

5. Application in timber engineering

5.1. Target camber

The amount of self-camber shall compensate for deflections of timber for TCC elements so that the requirements of serviceability limit states can be fulfilled. The target camber can be defined according to different requirements: (I) the short-term, elastic deflections of the timber slab during construction state caused by the self-weight of the timber element and fresh concrete in the case of TCC slabs; (II) the short-term, elastic deformations of the fully effective TCC slab caused by the self-weight and the dead load; and (III) the long-term deflections of the TCC slab caused by the self-weight, the dead load and the permanent part of the live load.

In the following, the calculation of the target camber for the three different states mentioned above is shown for a TCC slab. The deflections are calculated according to Swiss standards SIA 265 [33], Eurocode 5 (EC5) [37] and the technical specification for TCC complementing EC5 [13]. The required limit values are calculated according to SIA 260 [38]. The static system for all considered cases is taken as a single-span, simply supported beam with constant cross-sections and material properties, and the load is uniformly distributed. The deflections are:

$$w(q) = \frac{5ql^4}{384EI}. \tag{21}$$

The target camber value $w(c)_{req}$ results from the deflection $w(q)$ and the admissible limit values w_{adm}:

$$w(c)_{req} = w(q) - w_{adm}. \tag{22}$$

(I) Target camber for construction state

In the construction state of an in-situ produced TCC slab, the timber cross-section carries the self-weight of the timber and the in-situ concrete casting. An additional dead load of $q_C = 1\,\mathrm{kN/m^2}$ is considered for loads during construction, e.g. construction workers or building materials. The total load on the slab is:

$$q_{tot,I} = \rho_{k,t} \cdot bh_t + \gamma_{c,f} \cdot bh_c + q_C, \tag{23}$$

where $\rho_{k,t}$ is the characteristic density of timber, $\gamma_c = 25\,\mathrm{kN/m^3}$ the density of concrete, b the width of the slab, h_t the height of the timber cross-section, h_c the height of the concrete cross-section, and q_C the load during construction. The structural effective cross-section is the timber cross-section. Hereby, the effective height of the timber is conservatively considered as:

$$h_{t,red} = h_t - h_{in}, \tag{24}$$

where h_{in} is the depth of cut for inlay as illustrated in Fig. 2. The flexural rigidity for state I is then:

$$EI_I = E_t \cdot \frac{bh_{t,red}^3}{12}, \tag{25}$$

where E_t is the modulus of elasticity of timber. The admissible deflection for this case is $w_{adm,I} = 0\,\mathrm{mm}$. Using the calculations above, results for deflections and required target camber for TCC slabs of 1 m width and varying spans are summarized in Table 5. The different spans (l = 4, 6, 8, and 10 m) are chosen according to practical spans encountered in most situations of housing or office buildings.

(II) Target camber for a slab at the beginning of service life

At the beginning of service life, assuming that the slab is either supported during construction or that the deflections are fully compensated by camber, the slab will deflect under the following components: Self-weight of the timber and the concrete, and dead load of the ceiling structure q_A. Under certain circumstances it may also be necessary to include a part of the live load q_N, representing e.g. the furniture in an office building. In the following calculation it is assumed that this part is the frequent part of the live load ψ_1. The total load on the slab is therefore:

Table 5
Target camber for TCC slabs of 1 m width during construction state (I). The geometric properties (e.g. concrete heights for each span) also apply for Tables 6 and 7.

Parameter	Label	Unit	Span l			
			4 m	6 m	8 m	10 m
Concrete height	h_c	[mm]	80	80	100	150
Timber height	h_t	[mm]	120	120	200	240
Depth of cuts	h_{in}	[mm]	35	40	55	60
Eff. timber height	$h_{t,red}$	[mm]	85	80	145	180
Flexural rigidity	EI_I	[kNm^2]	563	469	2795	5346
Total load	$q_{tot,I}$	[kN/m^2]	3.6	3.6	4.5	6.0
Deflection	$w(q)_I$	[mm]	21	129	86	145
Target deflection	$w_{adm,I}$	[mm]	0	0	0	0
Target camber	$w(c)_{req,I}$	[mm]	21	129	86	145

$$q_{tot,II} = \rho_{k,t} \cdot bh_t + \gamma_c \cdot bh_c + q_A + \psi_1 \cdot q_N, \tag{26}$$

where $\gamma_c = 25\,\mathrm{kN/m^3}$ is the density of hardened concrete, q_A the dead load, ψ_1 the coefficient of frequent part of the live load, and q_N the live load.

For state II, the structural effective cross-section is the composite TCC section. The effective flexural rigidity EI_{eff} is determined with the γ-method described in Eurocode 5, Annex B [37]. For the connection between timber and concrete in this example, a micro-notch system [39,40] is chosen with slip modulus $K = 880\,\mathrm{kN/mm/m}$ and a conservative effective distance between the micro-notch strips of $s = 900\,\mathrm{mm}$. The reduction factor γ considering the connection stiffness calculates as:

$$\gamma_{II} = \frac{1}{1 + \frac{\pi^2 E_c A_c s}{K l^2}}, \tag{27}$$

where E_c is modulus of elasticity of concrete and A_c the area of the concrete cross-section: $A_c = bh_c$. The distance z between the centroids of timber and concrete is:

$$z = \frac{h_c}{2} + h_{in} + \frac{h_{t,red}}{2}, \tag{28}$$

and the distances between the centroids of each component and the reference axis, namely the axis of zero stresses in timber, are:

$$a_{c,II} = \frac{A_t z}{\gamma_{II} n_c A_c + A_t}, \tag{29}$$

$$a_{t,II} = \frac{\gamma_{II} n_c A_c z}{\gamma_{II} n_c A_c + A_t}. \tag{30}$$

where A_t is area of the timber cross-section: $A_t = bh_{t,red}$ and n_c is ratio of moduli of elasticity $\frac{E_c}{E_t}$. The effective flexural rigidity is then

$$EI_{II} = E_t \cdot \left(n_c I_c + I_t + \gamma_{II} n_c A_c a_c z\right). \tag{31}$$

where I_c is the moment of inertia of concrete and I_t is the moment of inertia of timber. As for state I, the target deflection for state II is $w_{adm,II} = 0\,\mathrm{mm}$. Table 6 shows the deflections and the required target camber values for the different spans l.

(III) Target camber at the end of service life

According to Swiss standard SIA 260 [38], two serviceability limit states at the end of the service life shall be verified: The functioning and the appearance of the structure or structural members under normal use. The limit state concerning the functioning is affected by the deformations of the structure after completion of the considered installations. In this case no camber can be applied. However, camber can be applied to the limit state concerning the appearance. In this limit

Table 6
Target camber for TCC slabs of 1 m at the beginning of service life (II).

Parameter	Label	Unit	Span l			
			4 m	6 m	8 m	10 m
γ-value	γ_{II}	[–]	0.382	0.582	0.662	0.674
Flexural rigidity	EI_{II}	[kNm²]	8531	9802	34177	76514
Total load	$q_{tot,II}$	[kN/m²]	5.9	5.9	6.8	8.3
Deflection	$w(q)_{II}$	[mm]	2	10	11	14
Target deflection	$w_{adm,II}$	[mm]	0	0	0	0
Target camber	$w(c)_{req,II}$	[mm]	2	10	11	14

state, the permanent and quasi-permanent loads are considered. The total load on the slab is:

$$q_{tot,III} = \rho_{k,t} \cdot bh_t + \gamma_c \cdot bh_c + q_A + \psi_2 \cdot q_N, \tag{32}$$

where ψ_2 is the coefficient of quasi-permanent part of the live load. The structural effective cross-section is the composite section, subjected to long-term effects. The effective flexural rigidity EI_{eff} is determined, as before, with the γ-method described in Eurocode 5, Annex B [37]. However, the long-term effects are taken into account according to the technical specification for TCC [13]. To take into account the influence of creep, the moduli of elasticity of timber, concrete, and the connection are reduced with a material-specific creep factor φ_i and a connection and material-specific coefficient ψ_i:

$$E_{c,\infty} = \frac{E_c}{1 + \psi_{conc} \cdot \varphi_c}, \tag{33}$$

$$E_{t,\infty} = \frac{E_t}{1 + \psi_{timb} \cdot \varphi_t}, \tag{34}$$

$$K_{\infty} = \frac{K}{1 + \psi_{conn} \cdot \varphi_{conn}}. \tag{35}$$

In the calculation of deflections for state III, the creep factors were chosen for concrete as $\varphi_c = 2.5$, for timber as $\varphi_t = 0.6$, and for the connection as $\varphi_{conn} = 2 \cdot \varphi_t$. The connection and material-specific coefficients ψ_i are determined using γ_{II} and Table 7.1 from the technical specification document [13]. Using the reduced moduli of elasticity and slip modulus from Eqs. (33) to (35), the γ-method (Eqs. (27) to (31)) results in an effective flexural rigidity considering long-term creep effects $EI_{III,creep}$. In a next step, the influence of shrinkage is considered by both an additional fictitious load p_{sls} and a further reduction of the effective flexural rigidity. The fictitious load p_{sls} is determined by the strain caused by shrinkage ε_{sls} as:

$$p_{sls} = C_{p,sls} \cdot \varepsilon_{sls}, \tag{36}$$

with

$$C_{p,sls} = \pi^2 \cdot \frac{E_c A_c E_t A_t z \gamma_{III}}{(E_c A_c + E_t A_t) l^2}. \tag{37}$$

The effective flexural rigidity considering shrinkage is:

$$EI_{III,sls} = C_{j,sls} \cdot E_{III,creep}, \tag{38}$$

with

$$C_{j,sls} = \frac{p_{sls} + q_{tot,III}}{\frac{E_c A_c + E_t A_t}{\gamma_{III} E_t A_t + E_c A_c} \cdot p_{sls} + q_{tot,III}}. \tag{39}$$

Finally, the total deflection at the end of the service life time considering creep and shrinkage is then calculated as:

$$w(q)_{III} = \frac{5(q_{tot,III} + p_{sls}) l^4}{384 EI_{eff,S}}. \tag{40}$$

The target deflection for this case is $w_{adm,III} = l/300$ according to SIA 265 [38]. Table 7 summarizes the deflections and the required target camber values for different spans l considering the long-term effects during a service life of 50 years.

Table 7
Target camber for TCC slabs of 1 m at the end of service life (III).

Parameter	Label	Unit	Span l			
			4 m	6 m	8 m	10 m
γ-value$t = 0$	γ_{II}	[–]	0.382	0.582	0.662	0.674
Creep coefficient	ψ_{conc}	[–]	1.92	1.82	1.77	1.76
	ψ_{timb}	[–]	1.00	1.00	1.00	1.00
	ψ_{conn}	[–]	1.00	1.00	1.00	1.00
γ-value t = ∞	γ_{III}	[–]	0.620	0.779	0.830	0.835
Flexural rigidity	$EI_{III,creep}$	[kNm²]	3161	3668	12584	28473
Flexural rigidity	$EI_{III,sls}$	[kNm²]	2900	3542	12292	27788
Total load	$q_{tot,III}$	[kN/m²]	5.3	5.3	6.2	7.7
Shrinkage load	p_{sls}	[kN/m²]	4.5	2.6	3.6	3.8
Deflection	$w(q)_{III}$	[mm]	11	38	42	54
Target deflection	$w_{adm,III}$	[mm]	13	20	27	33
Target camber	$w(c)_{req,III}$	[mm]	0	18	15	21

5.2. Application of self-camber

The calculations above for target camber of different spans show that the effective height of the timber $h_{t,red}$ and the span l have the largest influence on the deflections and thus on the camber needed. For these examples of TCC slabs, state (I) during construction is the decisive state because the required target camber is by far the highest. It can generally be seen that for all investigated spans, the states II and III require a camber that is lower by an entire magnitude than that of state I. Comparing the required target camber for each of the situations and spans to the self-camber that can hypothetically be achieved based on model calculations (see Table 8 and Fig. 10), it can be concluded that:

- When the inlay orientation is T, for the inlay configuration given in Table 8, that $w(c) > w(c)_{req,I}$ for a span of 4 m, but not above.
- When the inlay orientation is R, $w(c) > w(c)_{req,I}$ for spans 4, 6 and 8 m, but not for 10 m.

Eq. (21) and (22) show that the target camber $w(c)_{req}$ increases disproportionally with span as the deflection is dependent on the span to the 4th power. However, the self-camber $w(c)$ is a measure to achieve a desired curvature and would not increase disproportionally with span. Therefore, it must be noted that for full compensation of the deflections for very large spans, the inlay configuration might need to be adjusted to a level where it is not economic or feasible anymore (e.g. too many inlays that are too closely spaced). Nevertheless, it can be shown in Fig. 10 that a large proportion of the deflections can be compensated with simple configurations of inlays.

It should be noted that the calculations of this section only address the serviceability limit state issue of TCC slabs using self-camber by swelling hardwood inlays exclusively in a proof-of-concept manner. The effect of the notches in the timber beam have not been assessed with respect to ultimate limit state. Further studies are needed in order to clarify aspects such as shear capacity or performance in combination with a shear connection between timber and concrete.

6. Conclusions

An innovative method to camber timber elements is presented in this paper to tackle the challenges of large deflections of timber–concrete composite beams during construction. An analytical model was derived in order to calculate the self-camber in dependence of geometry and material properties of the timber beam and the hardwood inlays. The model was shown valid for three samples of 2 m span spruce beams with varying geometrical configurations of oven-dried European beech inlays. A parametric study as well as a sensitivity analysis were conducted in order to assess use in practice. As a conclusion, self-camber was shown as an applicable concept for TCC slabs given some conditions, e.g. a low machining tolerance during manufacturing. For

Table 8
Model parameters and self-camber calculated from model for T and R oriented inlays, and target camber values for TCC slabs of 1 m width.

Parameter	Label	Unit	Span l			
			4 m	6 m	8 m	10 m
Timber height	h_t	[mm]	120	120	200	240
Depth of cuts	h_{in}	[mm]	35	40	55	60
Width of inlays	l_{in}	[mm]	35	40	55	60
Distance of inlays	d	[mm]	140	160	220	240
Distance to edge	l_R	[mm]	400	400	400	400
Number of inlays	l_R	[–]	19	27	27	31
Moisture change	$\Delta\omega$	[%]	10	10	10	10
Target camber I	$w(c)_{req,I}$	[mm]	21	129	86	145
Target camber II	$w(c)_{req,II}$	[mm]	2	10	11	14
Target camber III	$w(c)_{req,III}$	[mm]	0	18	15	21
Total Target camber	$w(c)_{req,tot}$	[mm]	23	157	112	180
Self-camber (model T)	$w(c)$	[mm]	29	72	58	67
Self-camber (model R)	$w(c)$	[mm]	58	142	115	131

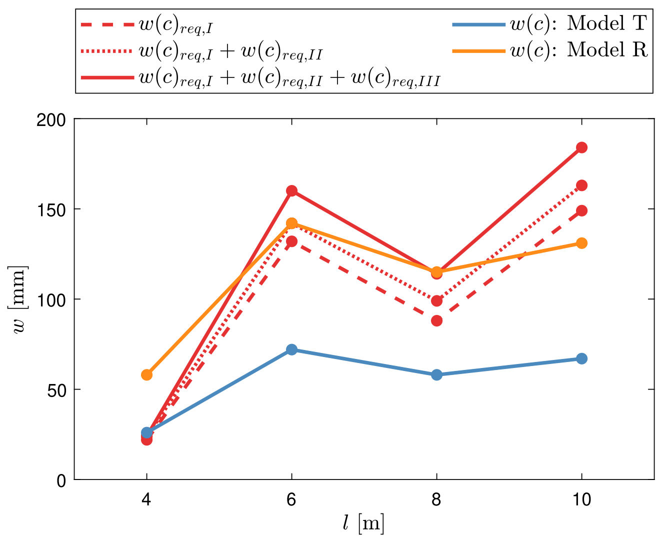

Fig. 10. Self-camber calculated from model for T and R oriented inlays, and target camber values for TCC slabs of 1 m, for spans of $l = 4$, 6, 8, and 10 m.

TCC slabs with self-cambered timber elements, it could be demonstrated that the expected deflections occurring over the service life of different span-scenarios can be compensated. Therefore, self-camber could represent a promising concept in timber engineering, but further experimental studies are still needed for validation and in order to investigate different spans or optimized inlay configurations.

CRediT authorship contribution statement

Katharina Müller: Formal analysis, Investigation, Methodology, Visualization, Writing - original draft, Conceptualization, Writing - review & editing. **Philippe Grönquist:** Formal analysis, Investigation, Methodology, Visualization, Writing - original draft, Conceptualization, Writing - review & editing. **Alex Sixie Cao:** Formal analysis, Visualization, Writing - review & editing. **Andrea Frangi:** Funding acquisition, Writing - review & editing.

Declaration of competing interest

The authors declare that they have no known competing financial interests or personal relationships that could have appeared to influence the work reported in this paper.

Acknowledgments

We sincerely thank Pius Herzog for help with the experiments, and Ingo Burgert for providing access to the climatic chamber. Sidler Holz AG is acknowledged for providing the timber and Innosuisse, Switzerland for the financial support (Project No. 25186.1 PFIW-IW). A patent related to the topic of this study is filed [41].

References

[1] M. Green, J. Taggart, Hoch Bauen Mit Holz, 2017, http://dx.doi.org/10.1515/9783035604788.
[2] M.H. Ramage, H. Burridge, M. Busse-Wicher, G. Fereday, T. Reynolds, D.U. Shah, G. Wu, L. Yu, P. Fleming, D. Densley-Tingley, J. Allwood, P. Dupree, P.F. Linden, O. Scherman, The wood from the trees: The use of timber in construction, Renew. Sustain. Energy Rev. 68 (2017) 333–359, http://dx.doi.org/10.1016/j.rser.2016.09.107.
[3] R.M. Andrew, Global CO_2 emissions from cement production, 1928 – 2018, Earth Syst. Sci. Data 11 (2019) 1675–1710.
[4] A.M.P.G. Dias, J. Skinner, K. Crews, T. Tannert, Timber-concrete-composites increasing the use of timber in construction, Eur. J. Wood Wood Prod. 74 (3) (2016) 443–451, http://dx.doi.org/10.1007/s00107-015-0975-0.
[5] Y. Plüss, D. Zwicky, Eco-Balance of Different Construction Methods in Timber and Concrete for Floor Slabs – a Case Study, in: Exploring the Potential of Hybrid Structures for Sustainable Construction, Hybrid2014 By Iabse.Ch, no. July, Fribourg, Switzerland, 2014.
[6] C. Martins, A.M.P.G. Dias, R. Costa, P. Santos, Environmentally friendly high performance timber-concrete panel, Constr. Build. Mater. 102 (2016) 1060–1069, http://dx.doi.org/10.1016/j.conbuildmat.2015.07.194.
[7] A. Frangi, Brandverhalten von Holz-Beton-Verbunddecken (Dissertation), ETH Zürich, 2001.
[8] D. Yeoh, M. Fragiacomo, M. De Franceschi, K.H. Boon, State of the art on timber-concrete composite structures: Literature review, J. Struct. Eng. 137 (10) (2011) 1085–1095, http://dx.doi.org/10.1061/(Asce)St.1943-541x.0000353.
[9] H.J. Blass, M. Schlager, Connections for Timber-Concrete-Composite Structures, IABSE Reports, Tech. Rep., International Association for Bridge and Structural Engineering, 1997, pp. 169–174, http://dx.doi.org/10.5169/seals-963.
[10] J. Schänzlin, Zum Langzeitverhalten von Brettstapel-Beton-Verbunddecken (Dissertation), Universität Stuttgart, 2003, p. 314.
[11] N. Khorsandnia, J. Schänzlin, H. Valipour, K. Crews, Time-dependent behaviour of timber-concrete composite members: Numerical verification, sensitivity and influence of material properties, Constr. Build. Mater. 66 (January) (2014) 192–208, http://dx.doi.org/10.1016/j.conbuildmat.2014.05.079.
[12] B. Shi, W. Liu, H. Yang, X. Ling, Long-term performance of timber-concrete composite systems with notch-screw connections, Eng. Struct. 213 (February) (2020) 110585, http://dx.doi.org/10.1016/j.engstruct.2020.110585.
[13] A.M.P.G. Dias, M. Fragiacomo, R. Harris, P. Kuklik, V. Rajcic, J. Schänzlin, Technical specification CEN/TC 250/SC 5, TS TCC, final draft, 2020.
[14] M. Fragiacomo, J. Schänzlin, Proposal to account for concrete shrinkage and environmental strains in design of timber-concrete composite beams, J. Struct. Eng (United States) 139 (1) (2013) 162–167, http://dx.doi.org/10.1061/(ASCE)ST.1943-541X.0000605.
[15] M. Fragiacomo, E. Lukaszewska, Influence of the construction method on the long-term behavior of timber-concrete composite beams, J. Struct. Eng. 141 (10) (2015) 04015013, http://dx.doi.org/10.1061/(ASCE)ST.1943-541X.0001247.
[16] APA – The Engineered Wood Association, Glulam beam camber - Form no. S550H, 2015.
[17] F. Kupferle, A.M.P.G. Dias, W. Sebastian, J. Schänzlin, M. Fragiacomo, M. Ferreira, COST action FP1402 training school on TCC, (April) 2018.
[18] I. Giongo, M. Piazza, R. Tomasi, Cambering of timber composite beams by means of screw fasteners, J. Heritage Conserv. 32 (2012) 133–136.
[19] I. Giongo, G. Schiro, D. Riccadonna, Innovative pre-stressing and cambering of timber-to-timber composite beams, Compos. Struct. 226 (2019) 111195, http://dx.doi.org/10.1016/j.compstruct.2019.111195.
[20] B. Anshari, Z.W. Guan, A. Kitamori, K. Jung, K. Komatsu, Structural behaviour of glued laminated timber beams pre-stressed by compressed wood, Constr. Build. Mater. 29 (2012) 24–32, http://dx.doi.org/10.1016/j.conbuildmat.2011.10.002.
[21] B. Anshari, Z.W. Guan, Q.Y. Wang, Modelling of glulam beams pre-stressed by compressed wood, Compos. Struct. 165 (2017) 160–170, http://dx.doi.org/10.1016/j.compstruct.2017.01.028.
[22] B. Anshari, Z. Guan, FE modelling of optimization on strengthening glulam timber beams by using compressed wood blocks, Procedia Eng. 171 (2017) 857–864, http://dx.doi.org/10.1016/j.proeng.2017.01.379, The 3rd International Conference on Sustainable Civil Engineering Structures and Construction Materials - Sustainable Structures for Future Generations.
[23] K. Laine, T. Belt, L. Rautkari, J. Ramsay, C.A.S. Hill, M. Hughes, Measuring the thickness swelling and set-recovery of densified and thermally modified scots pine solid wood, J. Mater. Sci. 48 (24) (2013) 8530–8538, http://dx.doi.org/10.1007/s10853-013-7671-4.

[24] P. Grönquist, T. Schnider, A. Thoma, F. Gramazio, M. Kohler, I. Burgert, M. Rüggeberg, Investigations on densified beech wood for application as a swelling dowel in timber joints, Holzforschung 73 (6) (2019) 559–568, http://dx.doi.org/10.1515/hf-2018-0106.
[25] P. Grönquist, K. Müller, L. Imfeld, A. Frangi, Self-camber for Timber-concrete Composite Elements by Swelling Inlays: A Parametric Study, in: Proceedings of the World Conference on Timber Engineering WCTE 2021, Santiago, Chile, 2021.
[26] S. Fortino, F. Mirianon, T. Toratti, A 3D moisture-stress FEM analysis for time dependent problems in timber structures, Mech. Time-Depend. Mater. 13 (4) (2009) 333–356, http://dx.doi.org/10.1007/s11043-009-9103-z.
[27] M.M. Hassani, F.K. Wittel, S. Hering, H.J. Herrmann, Rheological model for wood, Comput. Methods Appl. Mech. Engrg. 283 (2015) 1032–1060, http://dx.doi.org/10.1016/j.cma.2014.10.031.
[28] R.L. Hankinson, Investigation of crushing strength of spruce at varying angles of grain, U.S. Air Serv. Inf. Circ. 3 (259) (1921).
[29] S. Hering, S. Saft, E. Resch, P. Niemz, M. Kaliske, Characterisation of moisture-dependent plasticity of beech wood and its application to a multi-surface plasticity model, Holzforschung 66 (3) (2012) 373–380, http://dx.doi.org/10.1515/hf.2011.162.
[30] W. Ramberg, W.R. Osgood, Description of Stress-Strain Curves by Three Parameters, Technical notes, U.S. National Advisory Committee for Aeronautics, 1943.
[31] N. Mostaghel, R.A. Byrd, Inversion of Ramberg–Osgood equation and description of hysteresis loops, Int. J. Non-Linear Mech. 37 (8) (2002) 1319–1335, http://dx.doi.org/10.1016/S0020-7462(02)00025-2.
[32] W. Olek, J. Majka, Ł. Czajkowski, Sorption isotherms of thermally modified wood, Holzforschung 67 (2) (2013) 183–191, http://dx.doi.org/10.1515/hf-2011-0260.
[33] SIA Swiss Society of Engineers and Architects, SIA 265: Holzbau, 2012.
[34] I.M. Sobol', Global sensitivity indices for nonlinear mathematical models and their Monte Carlo estimates, Math. Comput. Simulation 55 (1) (2001) 271–280, http://dx.doi.org/10.1016/S0378-4754(00)00270-6, The Second IMACS Seminar on Monte Carlo Methods.
[35] S. Marelli, B. Sudret, UQLab: A framework for uncertainty quantification in Matlab, in: Vulnerability, Uncertainty, and Risk, pp. 2554–2563. http://dx.doi.org/10.1061/9780784413609.257.
[36] S. Marelli, C. Lamas, K. Konakli, C. Mylonas, P. Wiederkehr, B. Sudret, UQLab User Manual – Sensitivity Analysis, Tech. rep. # UQLab-V1.4-106, Chair of Risk, Safety and Uncertainty Quantification, ETH Zurich, Switzerland, 2021.
[37] C.E.N. European Committee for Standardization, EN 1995-1-1:2010 - Eurocode 5: Design of timber structures - Part 1-1: General - Common rules and rules for buildings, in: Eurocode 5, vol. 1, 2010, pp. 1–123.
[38] SIA Swiss Society of Engineers and Architects, SIA 260: Grundlagen der Projektierung von Tragwerken, 2013.
[39] K. Müller, Timber-Concrete Composite Slabs with Micro-Notches (Dissertation), ETH Zürich, 2020, http://dx.doi.org/10.3929/ethz-b-000474874.
[40] K. Müller, A. Frangi, Micro-notches as a novel connection system for timber-concrete composite slabs, Eng. Struct. 245 (2021) 112688, http://dx.doi.org/10.1016/j.engstruct.2021.112688.
[41] M. Muster, S. Zöllig, E. Sidler, Elevation of wooden elements, 2018, WO2018047041.